Supporting Information

Unveiling Bulk-to-Interface Electrolyte Regulation for Ultralong-Life Zn-Ion Batteries

Yinyan Deng, [a] Shuangtao Xu, [a] Zhiping Peng, [a] Linfeng Fei*[a] and Tao Wang*[a]

[a] Department of Polymer Materials and Engineering, School of Physics and Materials Science, Nanchang University, Nanchang 330031, China

*Corresponding author: feilinfeng@gmail.com; wangt0715@ncu.edu.cn

Experimental Section

Chemicals and materials: Zn (50 μm, 99.99%) and Cu foils (20 μm, 99%) were purchased from Hefei Zhengying Research Co., Ltd, followed by washing with deionized water and ethanol before use. Zinc sulfate ($ZnSO_4 \cdot 7H_2O$, 99.9%), methyl bromoacetate (98%) were purchased from Titan. 4,4'-Azobis(4-cyanovaleric acid) (ACVA, 98%), N-(3-(dimethylamino) propyl) methacrylamide (DMAPMA, 99%), 1,3-propanesulfonate (1,3-PS, 99%), tetrahydrofuran (THF, 99%), and polyvinylidene difluoride (PVDF) were purchased from Shanghai Macklin Biochemical Co., Ltd. Acetylene black (AB) and active carbon (AC) were purchased from Guangdong Canrd New Energy Technology. All chemicals were directly used unless otherwise denoted. Deionized water was obtained through a Millipore Gradient system, achieving a resistivity of 18.2 MΩ cm. PDP and OPDP were synthesized according to previous report (Fig. S1),[1] and their NMR spectra are provided in Fig. S4.

Synthesis of CBA-ester (quaternized intermediate):

CBA-ester was synthesized via a nucleophilic substitution reaction between DMAPMA and methyl bromoacetate. The synthesis route is shown in Fig. S1. Specifically, 4.256 g (25 mmol) of DMAPMA was dissolved in 15 mL of THF and transferred to a 50-mL three-neck round-bottom flask. Then, 5.736 g (37.5 mmol) of methyl bromoacetate was dissolved in 15 mL of anhydrous THF and added dropwise to the reaction flask with continuous stirring under an ice-water bath. The reaction was maintained for 6 h under the protection of nitrogen. White precipitate was collected by vacuum filtration and washed several times with acetone. The product was dried under vacuum at room temperature for 12 h to obtain the desired quaternized intermediate of CBA-ester. ^{1}H NMR (400 MHz, D_2O, δ, Fig. S2a): 5.71 (s, 1H), 5.46 (s, 1H), 4.31 (s, 2H), 3.80 (s, 3H), 3.64-3.56 (m, 2H), 3.37-3.31 (t, J = 7.2 Hz, 2H), 3.26 (s, 6H), 2.09-1.97 (m, 2H), 1.91 (s, 3H).

Synthesis of CBA:

CBA was obtained by the hydrolysis of CBA-ester in the presence of anion-exchange resin (strongly basic Type I, 717-type), so that the ester group was converted into carboxylate and the residual bromide ions were removed simultaneously. Prior to use, the resin was first soaked in a 10 wt.% NaCl solution for 24 h, followed by thorough washing with deionized water until the rinsing solution was clear. Subsequently, the resin was immersed in a 5 wt.% HCl solution for 4 h and washed again with deionized water for neutrality. The resin was finally treated with 10 wt.% NaOH solution for

12 h and then rinsed with deionized water for a neutral pH. For the hydrolysis reaction, CBA-ester and the pretreated resin were co-added in deionized water and stirred under an ice-water bath for 48 h. After the reaction, the resin was removed by vacuum filtration, and the filtrate was concentrated under reduced pressure at 5 °C to yield a transparent and viscous carboxybetaine monomer of CBA. ^{1}H NMR (400 MHz, D_2O, δ, Fig. S2b): 5.63 (s, 1H), 5.39 (s, 1H), 3.79 (s, 2H), 3.54-3.48 (m, 2H), 3.29-3.23 (t, J = 7.2 Hz, 2H), 3.13 (s, 6H), 2.01-1.87 (m, 2H), 1.84 (s, 3H).

Synthesis of OCBA:

OCBA was synthesized by a telomerization method (Fig. S1). Typically, 10.0 g of CBA, 50 mg of ACVA, and 0.2422 g of mercaptoethanol as the chain transfer agent were added into 60 mL of water. The reaction vessel was sealed after three cycles of freeze-degas-thaw, and then the telomerization was proceeded at 70 °C for 16 h. Afterward, the reaction solution was dialyzed within water at 60 °C for 3 days, followed by freeze-drying to obtain the OCBA powder. The number-average molar mass (M_n ~ 3.1 × 10^3 g mol^{-1}, D_p ~ 14) of OCBA was determined by size-exclusion chromatography (Waters 1515, calibrated with monodisperse poly(ethylene glycol) standards) using 1.0 M $NaNO_3$ aqueous solution as the eluent at a flow rate of 1.0 mL min^{-1}. The D_p of OCBA similar to that of OPDP is designed to minimize the influence of additive molecular weight. ^{1}H NMR (400 MHz, D_2O, δ, Fig. S3a): 3.81 (br, 2H), 3.67-3.43 (br, 2H), 3.14 (br, 8H), 2.14-1.60 (br, 4H), 1.11-0.80 (br, 3H).

Synthesis of PANI:

PANI was synthesized following a previous report.[2] Briefly, 0.9 mL of aniline (~99%, Titan) was dissolved in 37.1 mL of 1.0 M HCl (Sinopharm), followed by dropwise adding 12.3 mL of 1.0 M HCl which contained 0.56 g of ammonium persulfate (98.5%, Macklin) under ice-bath conditions. After stirring for 1 h, the resulting product was collected by filtration, washed thoroughly with deionized water and ethanol, and dried under vacuum at 60 ℃ overnight.

Electrolyte preparation:

The bare electrolyte (BE, 2 M) was prepared by dissolving $ZnSO_4 \cdot 7H_2O$ in deionized water. The electrolyte solutions containing OCBA were prepared by adding 0.5, 1, 2, 5, or 8 wt.% of OCBA into BE.

Electrode preparation and cell assembly:

PANI electrode was prepared by mixing PANI powder, AB, and PVDF at a weight ratio of 7:2:1 in N-methylpyrrolidone (NMP, Macklin) to form a uniform slurry. This slurry was evenly coated onto a carbon cloth (Guangdong Canrd New Energy Technology Co., Ltd) using a doctor blade and subsequently dried under vacuum at 80 ℃ for 12 h. Electrodes with a diameter of 12 mm were punched from the coated substrate. CR2032 coin full batteries were assembled with PANI cathode, Zn foil anode, and glass fiber membrane (Whatman) separator. Zn//Zn symmetric cells and Zn//Cu half-cells were constructed in the same coin cell format.

Characterization:

FTIR spectra were recorded using a PE/Spectrum II spectrometer. XPS measurements were performed on a Thermo Scientific K-Alpha system with Al Kα radiation, and all binding energies were referenced to the C 1s peak at 284.8 eV. Raman spectra were obtained with a WITec Alpha300R Raman microscope. SEM images were captured on a Thermo Scientific Scios 2 HiVac field-emission scanning electron microscope. XRD analyses were conducted using an Empyrean diffractometer equipped with Cu-Kα radiation (λ = 1.5418 Å). ^{13}C and ^{1}H NMR spectra were collected on a 400 MHz digital NMR spectrometer.

Electrochemical Measurements:

LSV, Tafel plots, CA, differential capacitance curves, EIS, and CV curves were measured on a CHI 660E electrochemical workstation (Chenhua Instrument Company, Shanghai, China). The Tafel plots were obtained using a three-electrode system with Zn plate as the working electrode, platinum foil as the counter electrode, and Ag/AgCl as the reference electrode. LSV was carried out at 1 mV s^{-1} using the three-electrode mode with Ag/AgCl reference electrode, and platinum foils were used both as the working electrode and counter electrode. CA measurements were examined on Zn//Zn symmetric cells by applying a constant overpotential of −150 mV for 400 s. Differential capacitance curves of Zn//Cu cells were acquired within a voltage range from 0 to 1.0 V. EIS tests were conducted with a voltage amplitude of 5 mV within the frequency range from 1 MHz to 0.1 Hz. The CV curves of Zn//PANI cells were obtained from 0.5 V to 1.5 V at a scan rate of 0.5 mV s^{-1}.

$t_{Zn^{2+}}$ was obtained according to the typical Evans method, as described in the following formula:

$$t_{Zn^{2+}} = \frac{I_S(\Delta V - I_0 R_0)}{I_0(\Delta V - I_S R_S)} \quad (1)$$

where I_0, I_s, R_0, and R_s represent the current density and charge transfer resistance before and after the polarization test, respectively. ΔV is the constant polarization potential applied for the CA tests, and 10 mV was used here.

To more accurately assess the CE of initial Zn^{2+} plating/stripping at the anode, CE_{avg} was obtained by the Aurbach protocol. Specifically, a Zn layer corresponding to the capacity of 5 mAh cm^{-2} was initially deposited onto a Cu substrate, followed by a full stripping to activate the electrode surface. Subsequently, another Zn layer corresponding to the capacity of 5 mAh·cm^{-2} was deposited to serve as the Zn reservoir. Repetitive cycles involving the plating and stripping at 1 mA cm^{-2} and 0.4 mAh cm^{-2} Zn were then carried out. After completing such 110 cycles, the entire Zn reservoir was stripped. The CE_{avg} was determined based on the following equation:

$$\mathrm{CE}_{avg} = \frac{nQ_s+Q_f}{nQ_s+Q_r} \quad (2)$$

Here, Q_r denotes the amount of Zn initially deposited onto the Cu electrode to serve as the Zn reservoir (i.e., 5 mAh cm^{-2}); Q_s represents the Zn quantity cycled per cycle (i.e., 0.4 mAh cm^{-2}) over the 110 cycles; Q_f refers to the total Zn stripped from the copper electrode at the final test stage.

EQCM-D measurements:

EQCM-D measurements were conducted using a QEM 401 instrument (Q-sense AB) coupled with a Pgutouch electrochemical workstation (IPS Elektroniklabor GmbH & Co. KG). Gold-coated quartz crystal sensors (Q-sense AB) with a fundamental resonance frequency of ~5 MHz and a mass sensitivity constant of 17.7 ng cm^{-2} Hz^{-1} were employed. Two-electrode mode was adopted for tests. During the EQCM-D tests with CV procedure, the voltage was swept from −0.6 V to 0.6 V at a scan rate of 50 mV s^{-1}. For galvanostatic measurements, a current density of 0.5 mA cm^{-2} was applied for 8 min.

Computational method:

Theoretical calculations were carried out by the $DMol^3$ module. The generalized gradient approximation (GGA) with Perdew–Burke–Ernzerhof (PBE) was set as exchange correlation function. Based on electron–ion–nucleus interactions, all core electrons were processed. The selection of double numerical plus d-functions (DND) was regarded as the basis set. The energy change of 2.0×10^{-5} Ha, maximum displacement of 0.005 Å, and self-consistent field density convergence of 10^{-5} were set. The convergence tolerances for maximum force and maximum step

size between optimization cycles were 0.004 Ha $Å^{-1}$ and 0.3 Å, respectively.

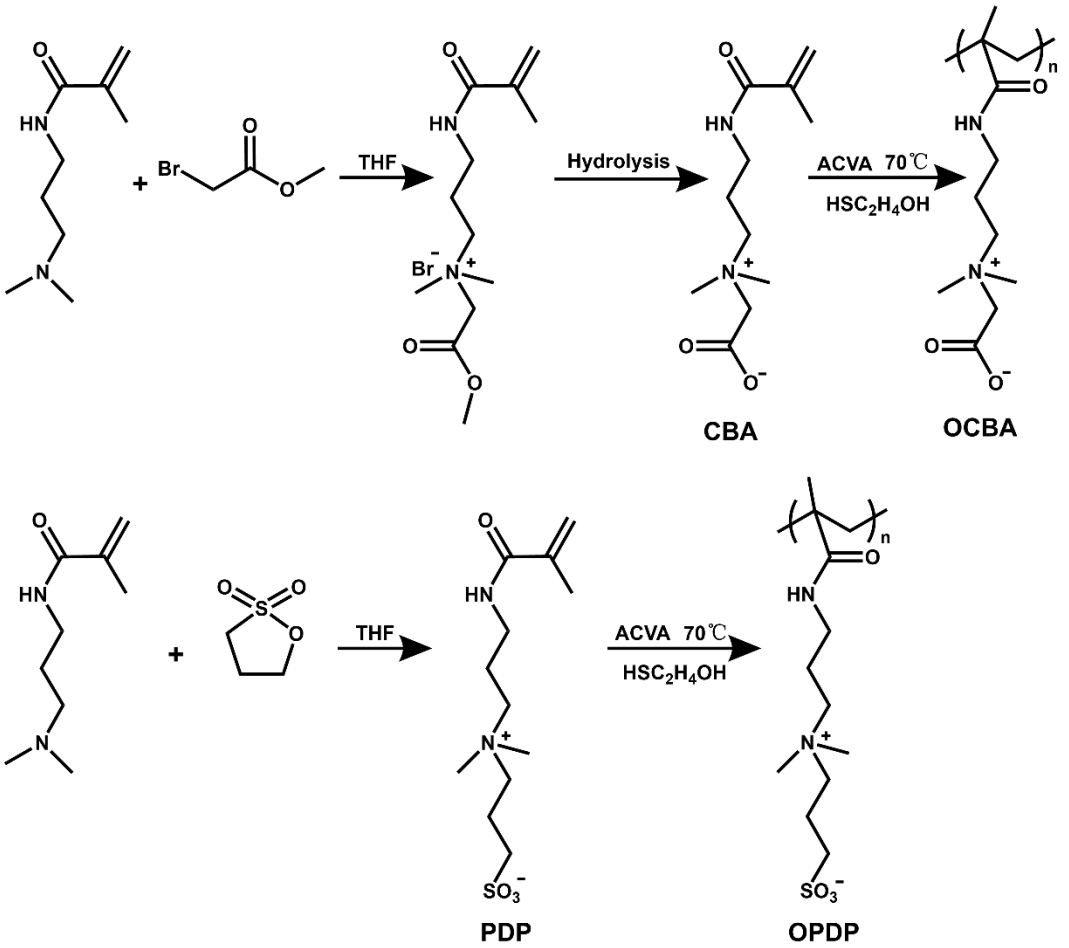

Fig. S1. The synthetic routes of zwitterionic monomers (CBA and PDP) and zwitterionic oligomer (OCBA and OPDP).

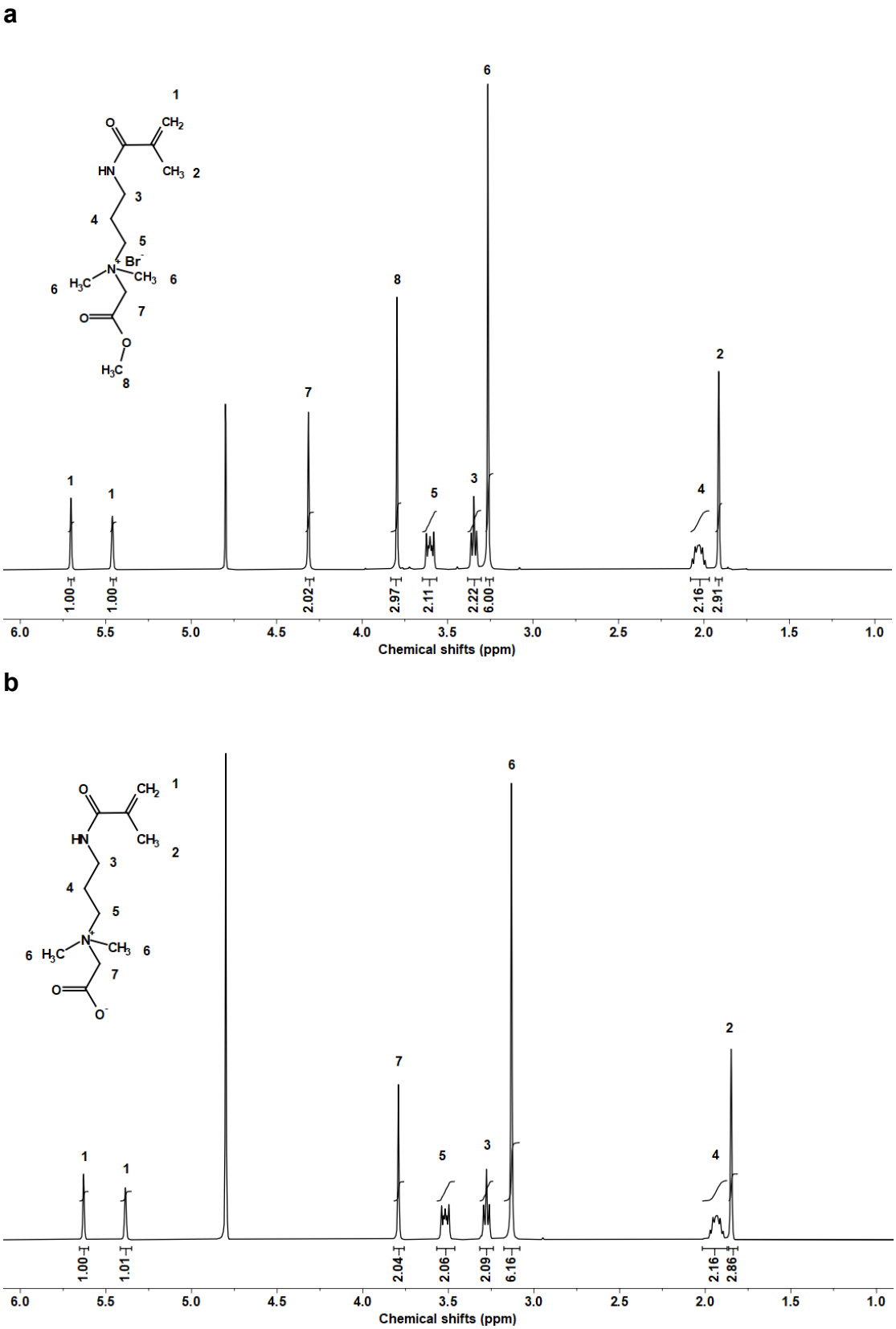

Fig. S2. ^{1}H NMR spectra of (a) CBA-ester and (b) CBA in D_2O.

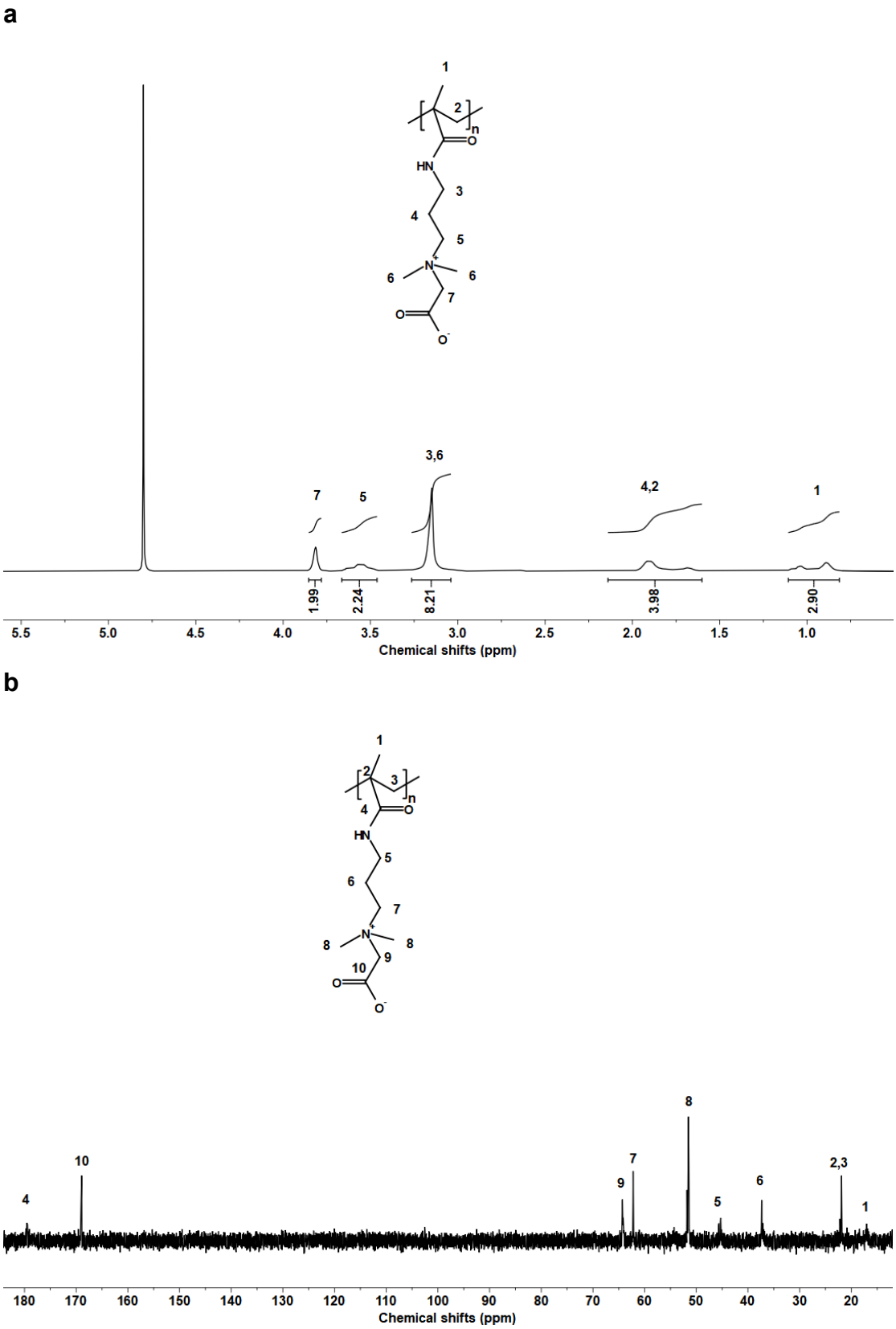

Fig. S3. (a) ^{1}H NMR and (b) ^{13}C NMR spectra of OCBA in D_2O.

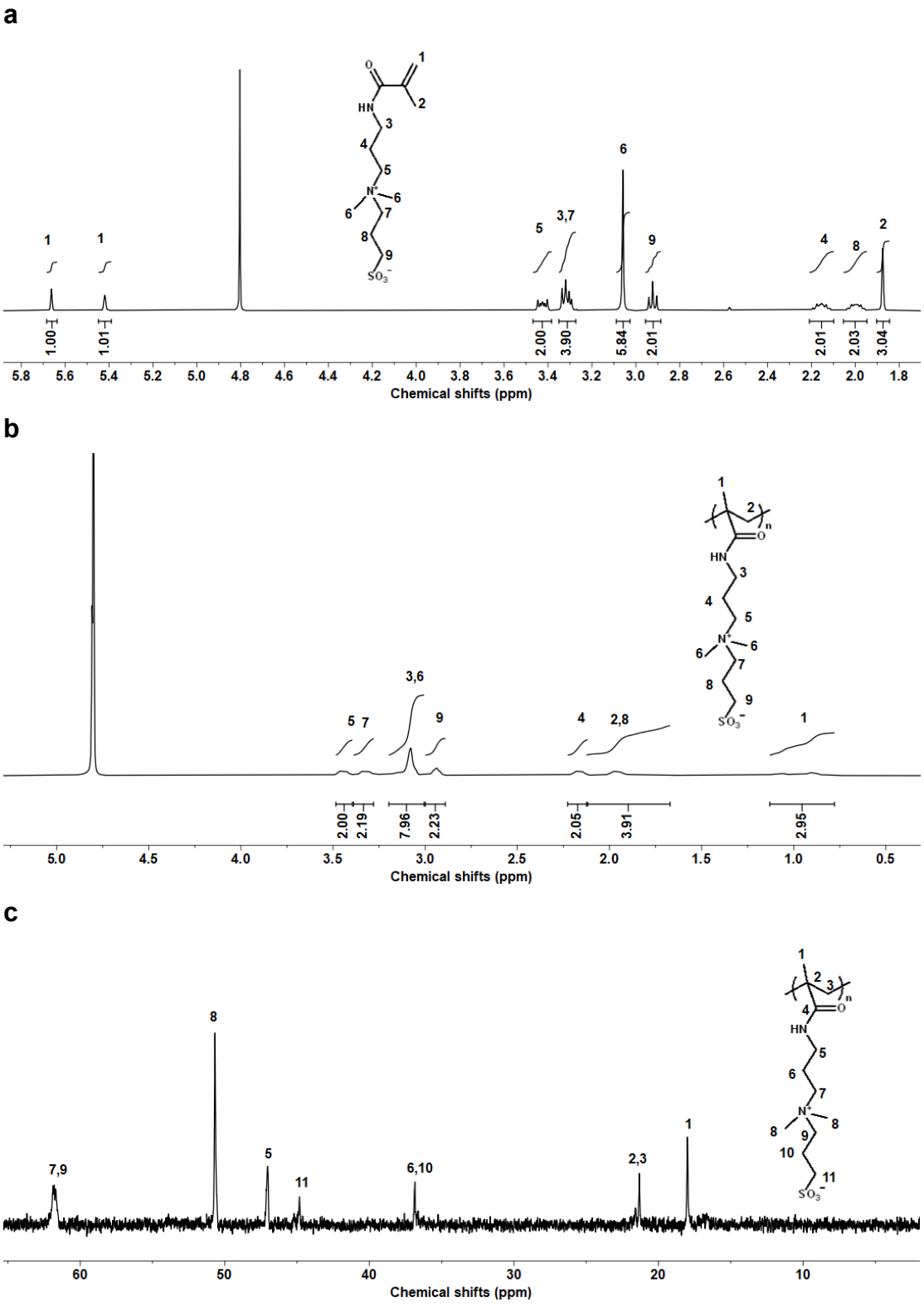

Fig. S4. ^{1}H NMR spectra of (a) PDP and (b) OPDP in D_2O. (c) ^{13}C NMR spectrum of OPDP in D_2O.

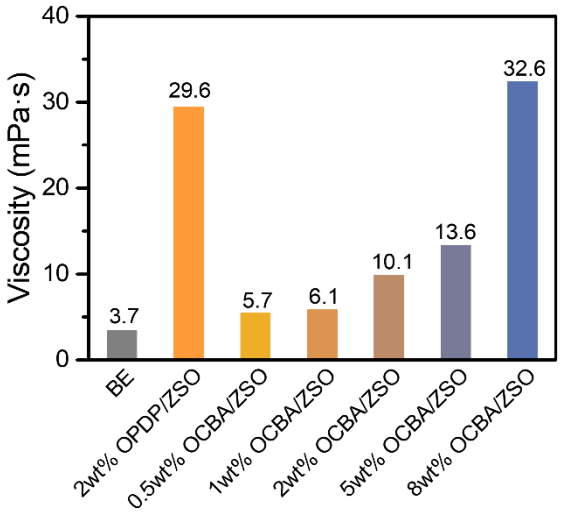

Fig. S5. Viscosity of electrolytes with different concentrations of OCBA/OPDP.

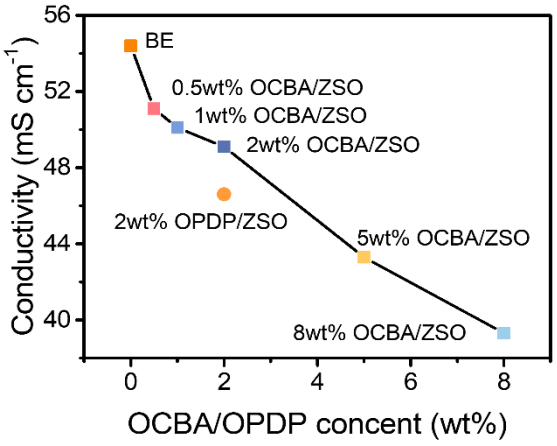

Fig. S6. Ionic conductivity of electrolytes with different concentrations of OCBA/OPDP.

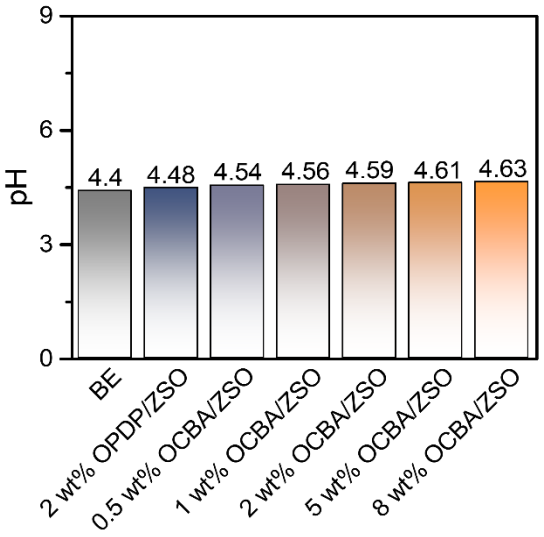

Fig. S7. pH of electrolytes with different concentrations of OCBA/OPDP.

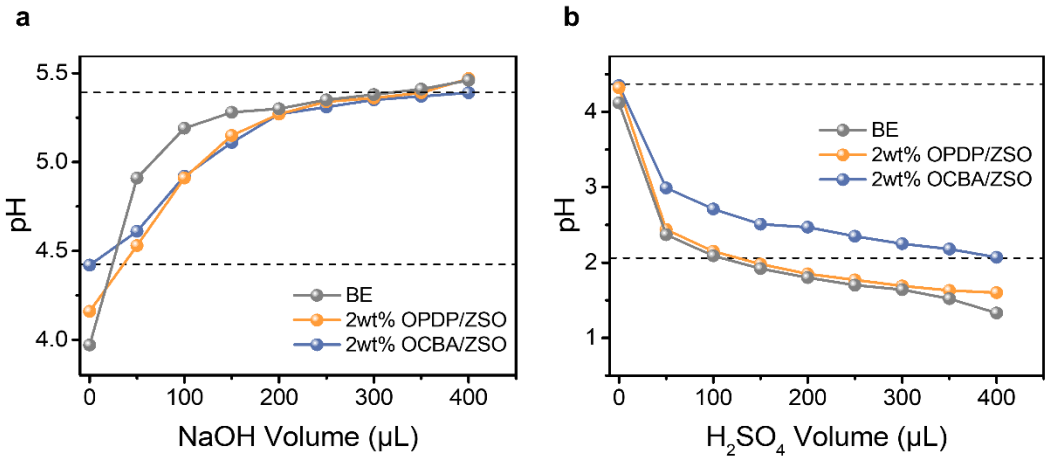

Fig. S8. (a) pH variations of different electrolytes under the titration of (a) 0.1 M NaOH and (b) 0.5 M H_2SO_4.

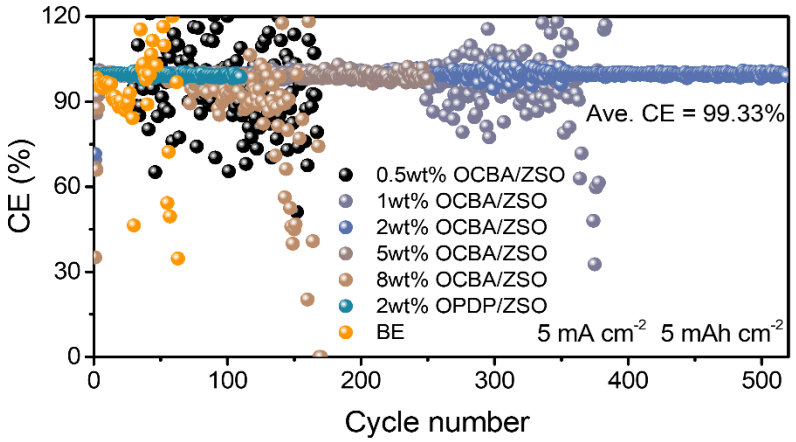

Fig. S9. Cycling performance of Zn//Cu batteries with different electrolytes at 5 mA cm^{-2} and 5 mAh cm^{-2}.

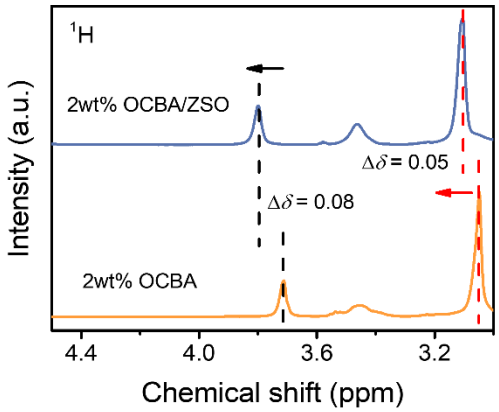

Fig. S10. ^{1}H NMR shifts of 2 wt% OCBA in D_2O with and without the addition of $ZnSO_4$.

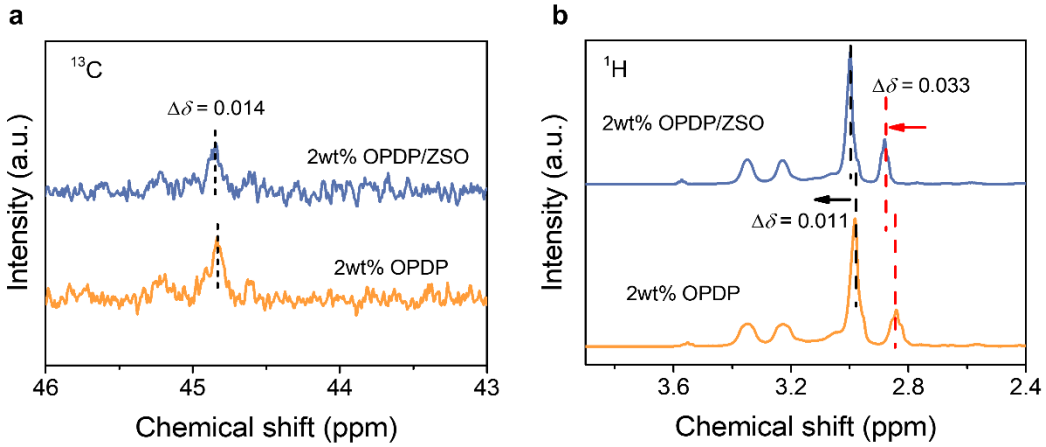

Fig. S11. ^{13}C NMR and ^{1}H NMR shifts of 2 wt% OPDP in D_2O with and without the addition of $ZnSO_4$.

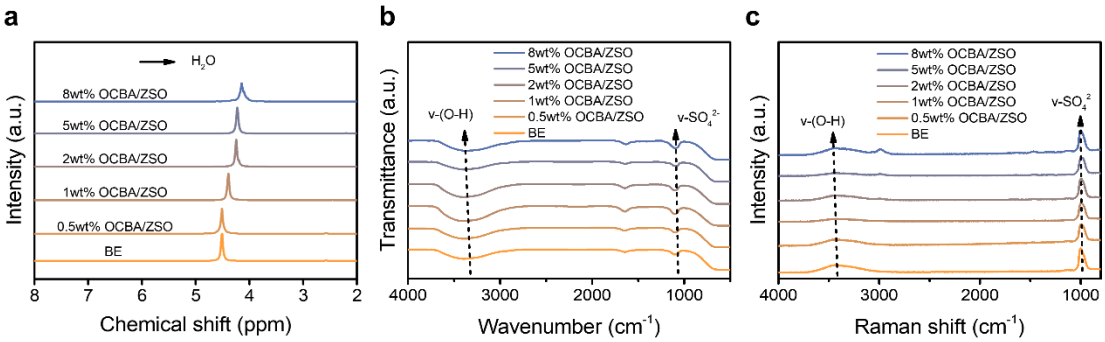

Fig. S12. (a) ^{1}H NMR shifts of H_2O, FTIR spectra, and Raman spectra of the OCBA-based electrolytes and BE.

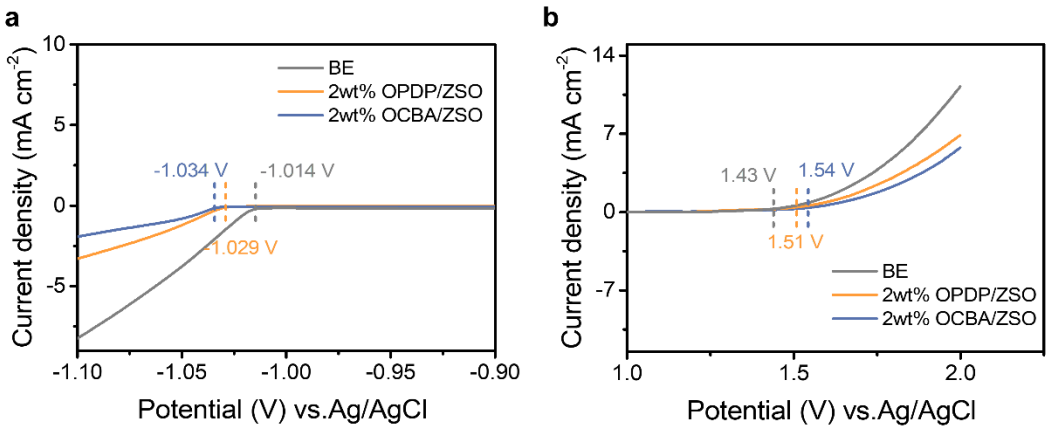

Fig. S13. Potentials of (a) HER and (b) OER in different electrolytes determined by LSV tests on Pt foil at a scan rate of 1 mV s^{-1}.

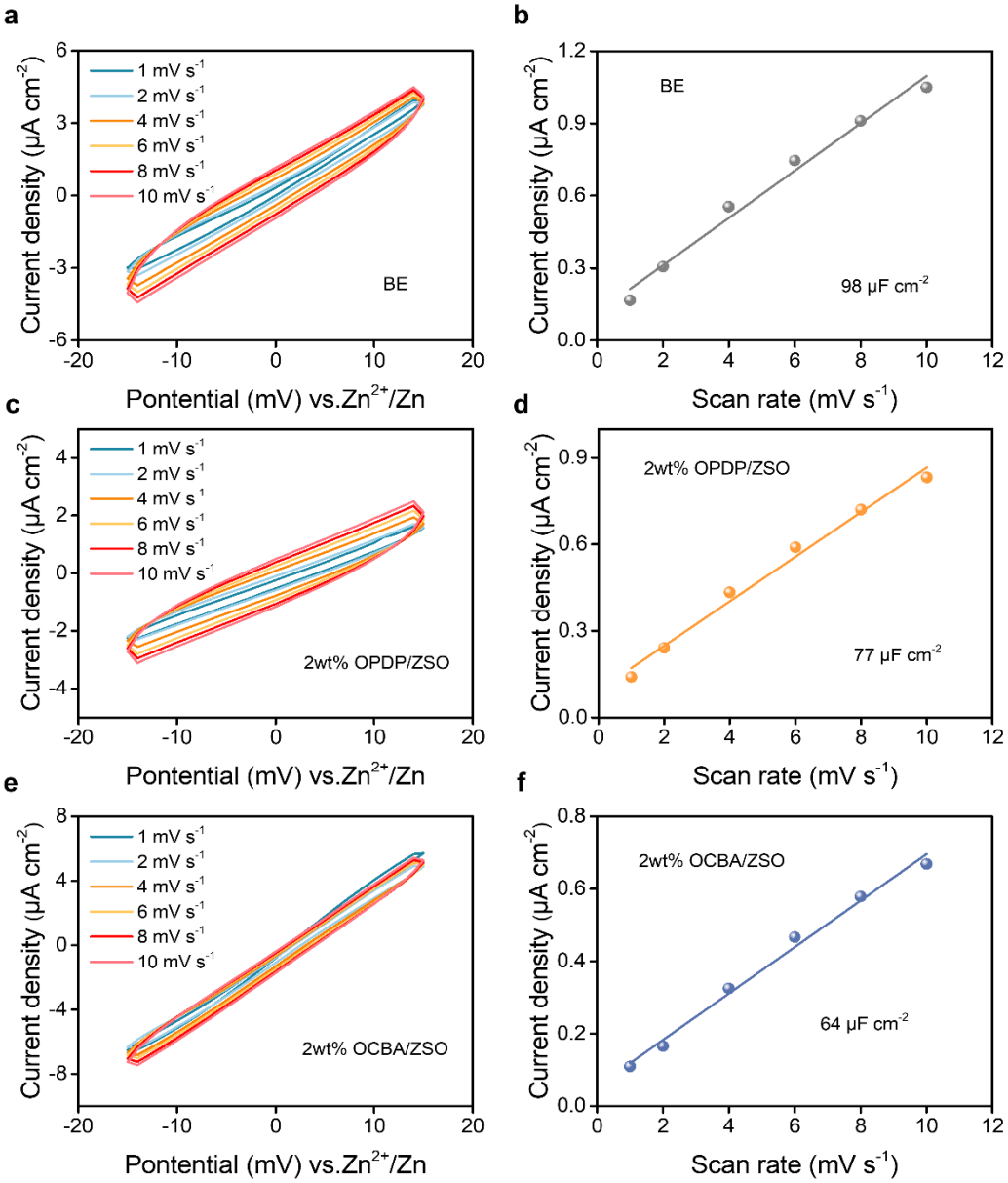

Fig. S14. Electric double layer capacitance (EDLC) measurements on Zn metals in different electrolytes. (a-e) CV curves of Zn//Zn symmetric cells with corresponding electrolytes in a voltage range from −15 mV to 15 mV under various scanning rates. (b-f) Plots of capacitive current versus scan rate for Zn//Zn symmetric cells with corresponding electrolytes.

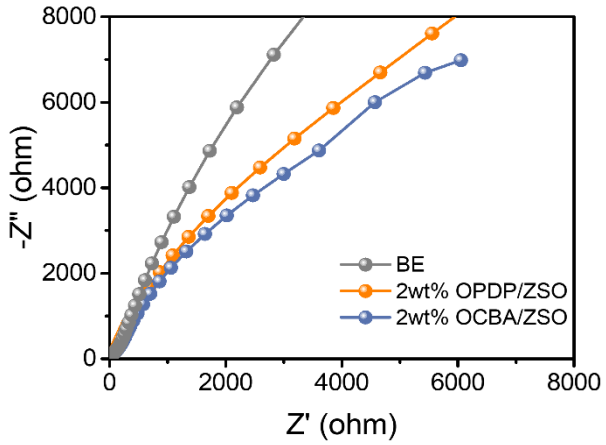

Fig. S15. EIS curves of Zn//Cu cells with different electrolytes.

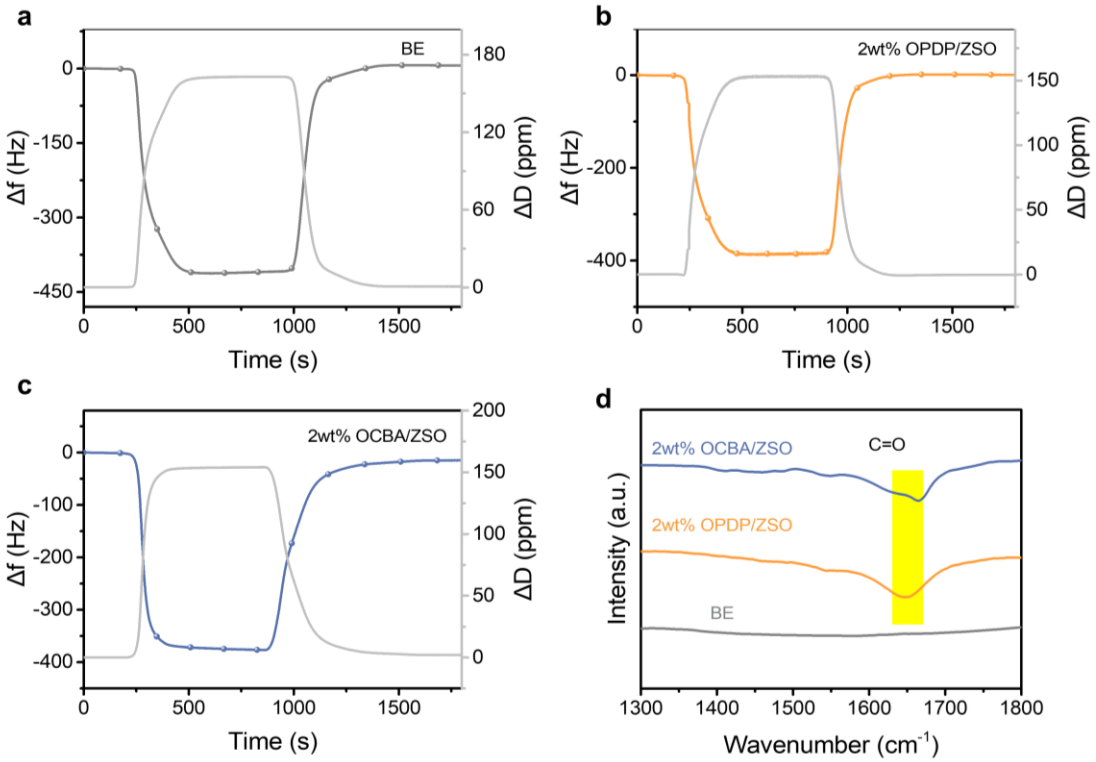

Fig. S16. (a-c) Time dependence of Δf and ΔD shifts during the adsorption and rinsing process of different electrolytes on the gold-coated sensor chips. (d) FTIR spectra for Zn foils after soaking in different electrolytes.

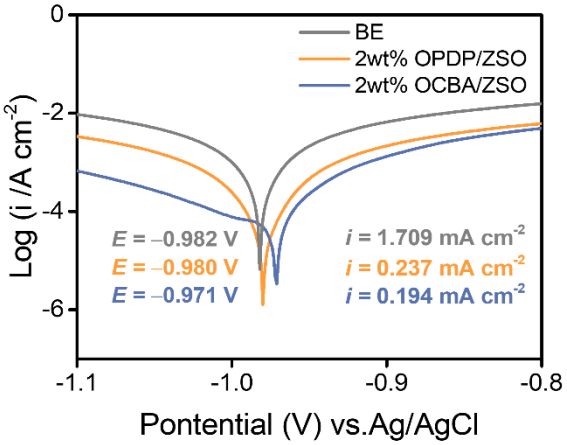

Fig. S17. Tafel curves of Zn anodes in different electrolytes.

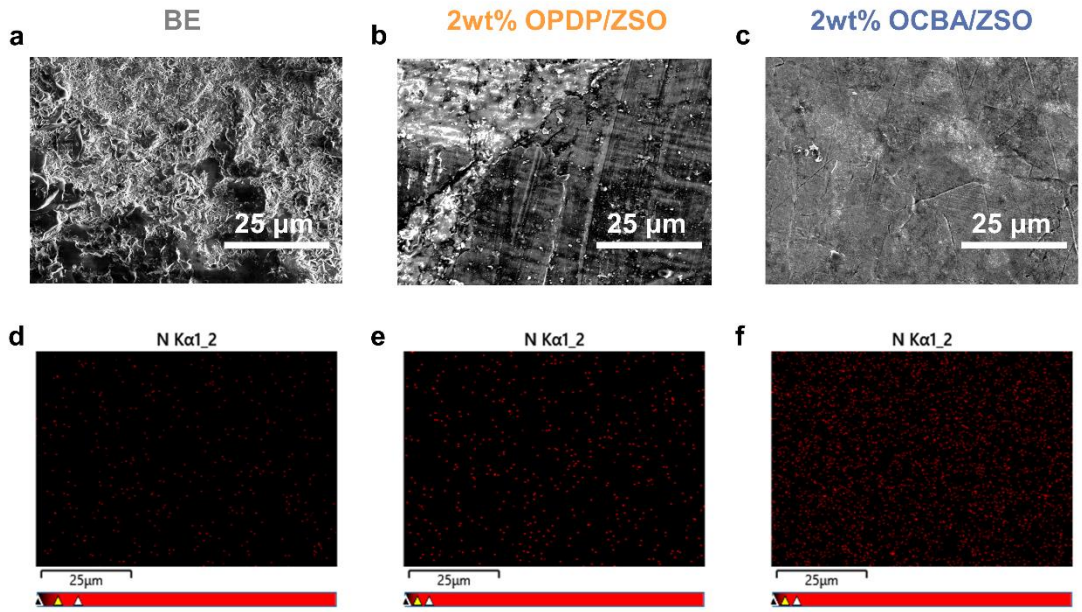

Fig. S18. SEM images of the Zn metals after immersed in (a) BE, (b)2 wt% OPDP/ZSO, and (c) 2 wt% OCBA/ZSO for 7 days. (d-f) EDS mapping results of N element on the Zn metals after immersed in different electrolytes.

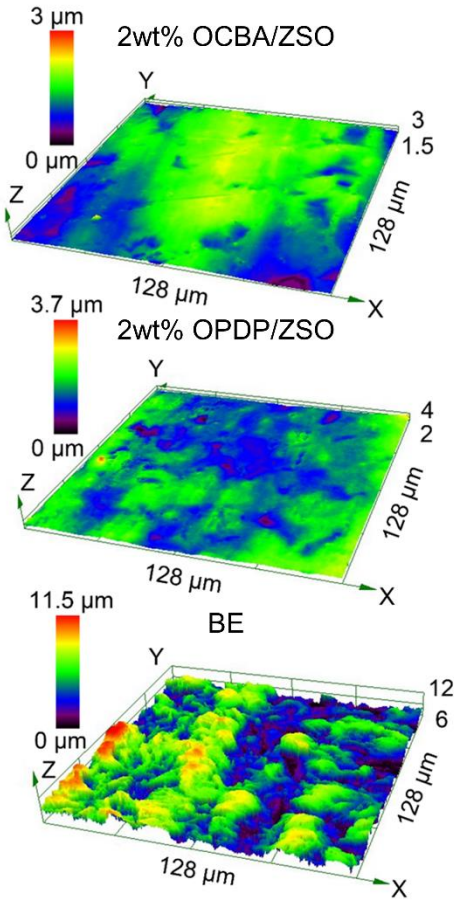

Fig. S19. CLSM images of the Zn metals after immersed in BE, 2 wt% OPDP/ZSO, and 2 wt% OCBA/ZSO for 7 days.

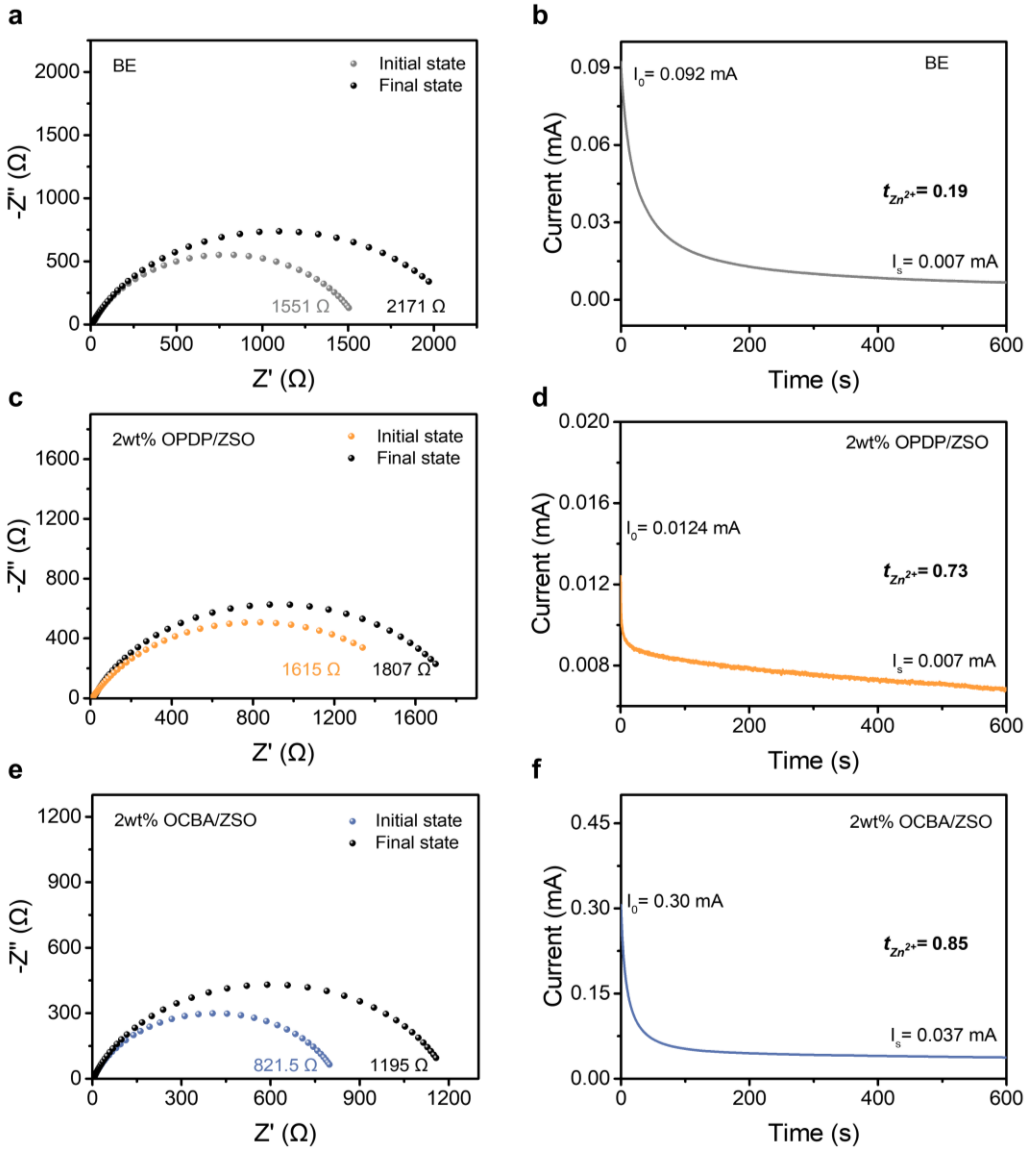

Fig. S20. (a, c, e) EIS plots of the Zn//Zn batteries with different electrolytes before and after polarization, and (b, d, f) the corresponding current-time plots during the polarization of batteries at a constant potential of 10 mV for 600 s. (a, b) BE; (c, d) 2 wt% OPDP/ZSO; (e, f) 2 wt% OCBA/ZSO.

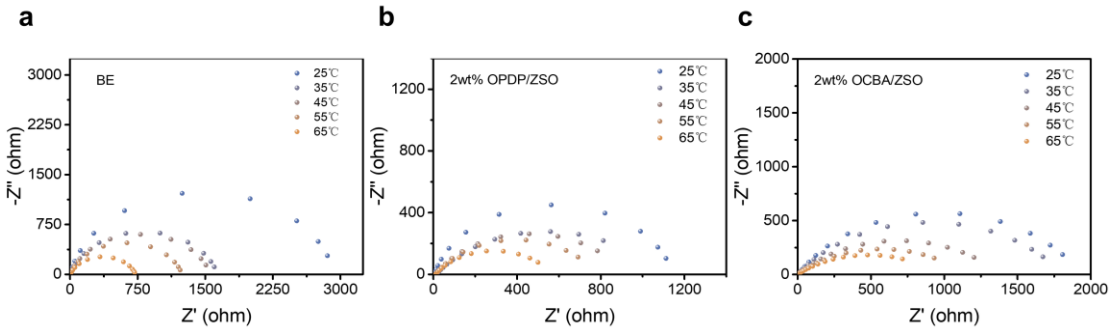

Fig. S21. EIS profiles of the Zn//Zn batteries with different electrolytes at a series of temperatures.

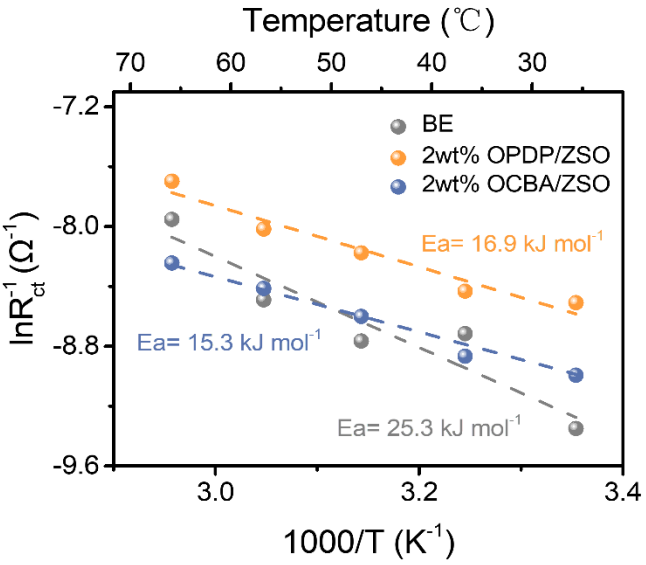

Fig. S22. Arrhenius curves and the obtained desolvation energy (E_a) of Zn^{2+} in different electrolytes.

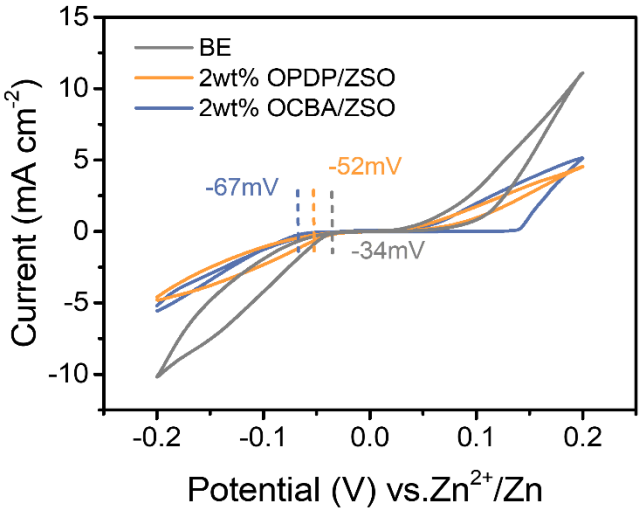

Fig. S23. CV curves of Zn//Cu cells in different electrolytes at 1 mV s^{-1}.

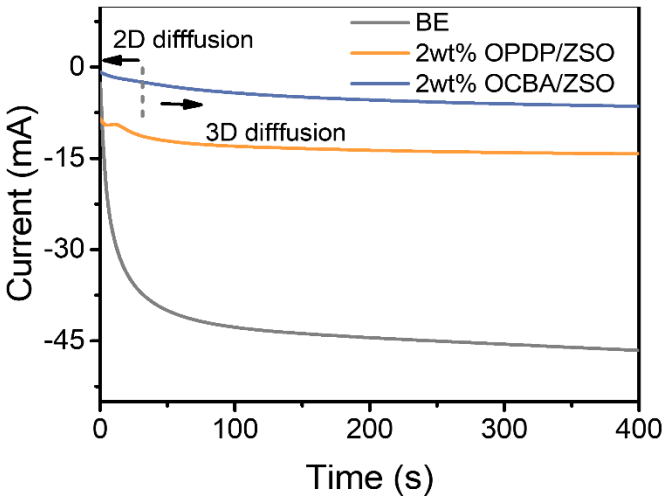

Fig. S24. Current-time plots of the Zn//Zn cells in different electrolytes at a fixed polarization potential of −150 mV.

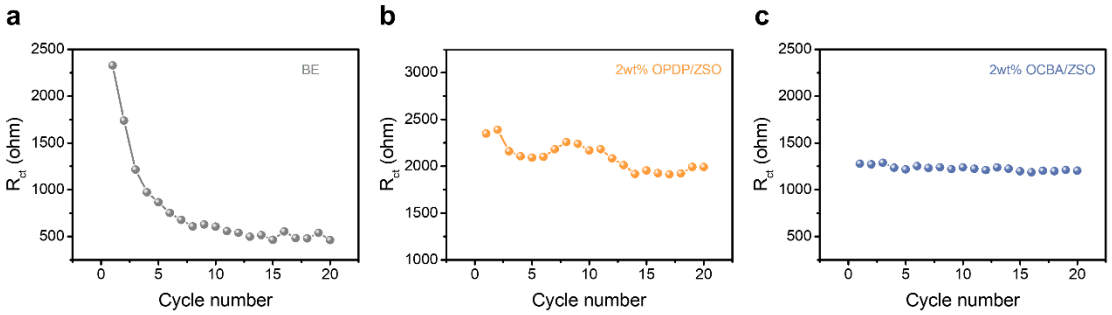

Fig. S25. R_{ct} variations from in situ EIS tests on the Zn//Zn symmetric cells at different cycles with (a) BE, (b) 2 wt% OPDP/ZSO, and (c) 2 wt% OCBA/ZSO electrolytes.

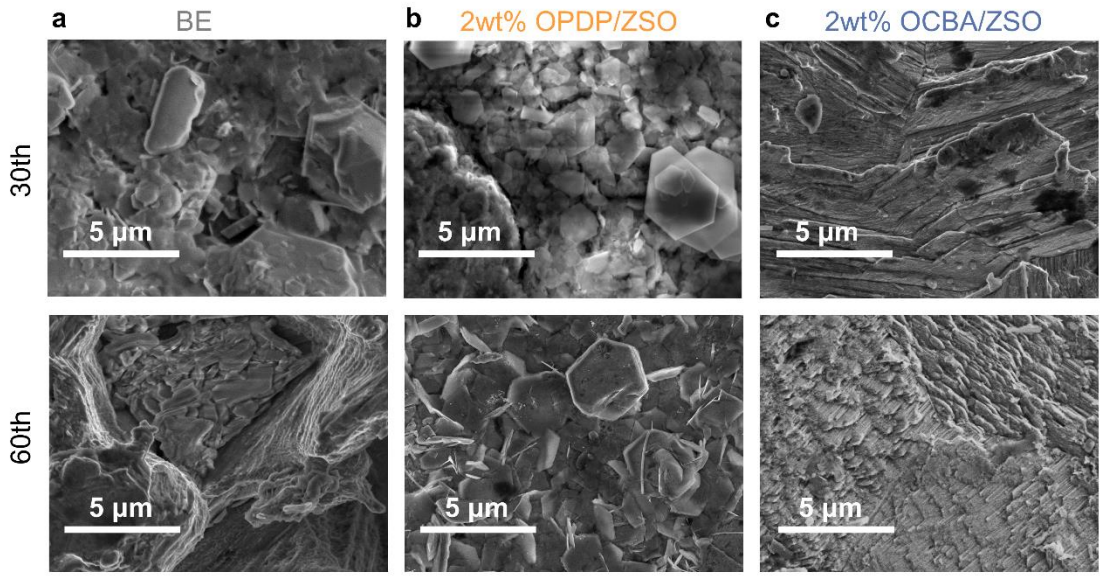

Fig. S26. SEM surface images of the Zn anodes after 30 and 60 charge/discharge cycles in (a) BE, (b) 2 wt% OPDP/ZSO, and (c) 2 wt% OCBA/ZSO electrolytes under the current density of 1 mA cm^{-2} and the capacity of 1 mAh cm^{-2}.

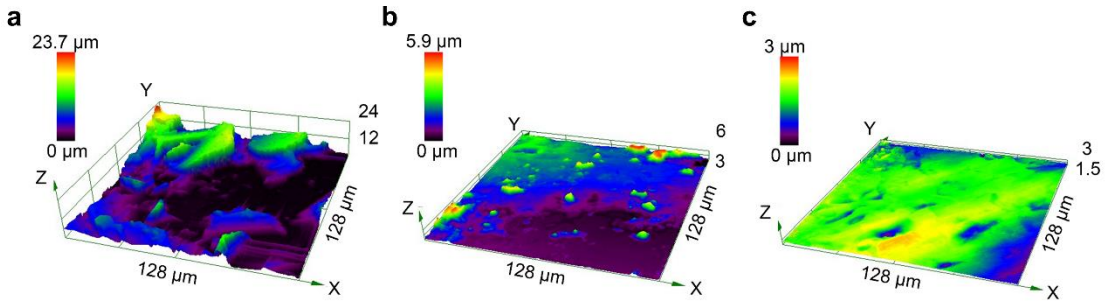

Fig. S27. 3D CLSM images of Zn anodes after 60 charge/discharge cycles in (a) BE, (b) 2 wt% OPDP/ZSO, and (c) 2 wt% OCBA/ZSO.

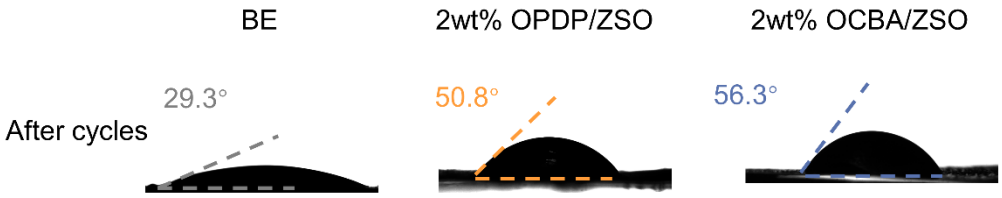

Fig. S28. Contact angles of different electrolytes on the Zn anodes after 60 cycles in the corresponding electrolyte.

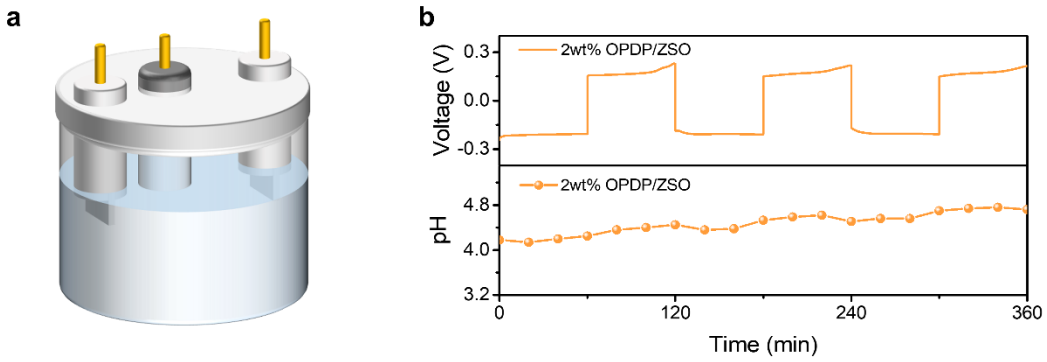

Fig. S29. (a) Schematics of the device for in-situ monitoring pH changes. (b) Time–voltage curves and real-time pH evolution near Zn anode in 2 wt% OPDP/ZSO electrolyte during the plating/stripping process.

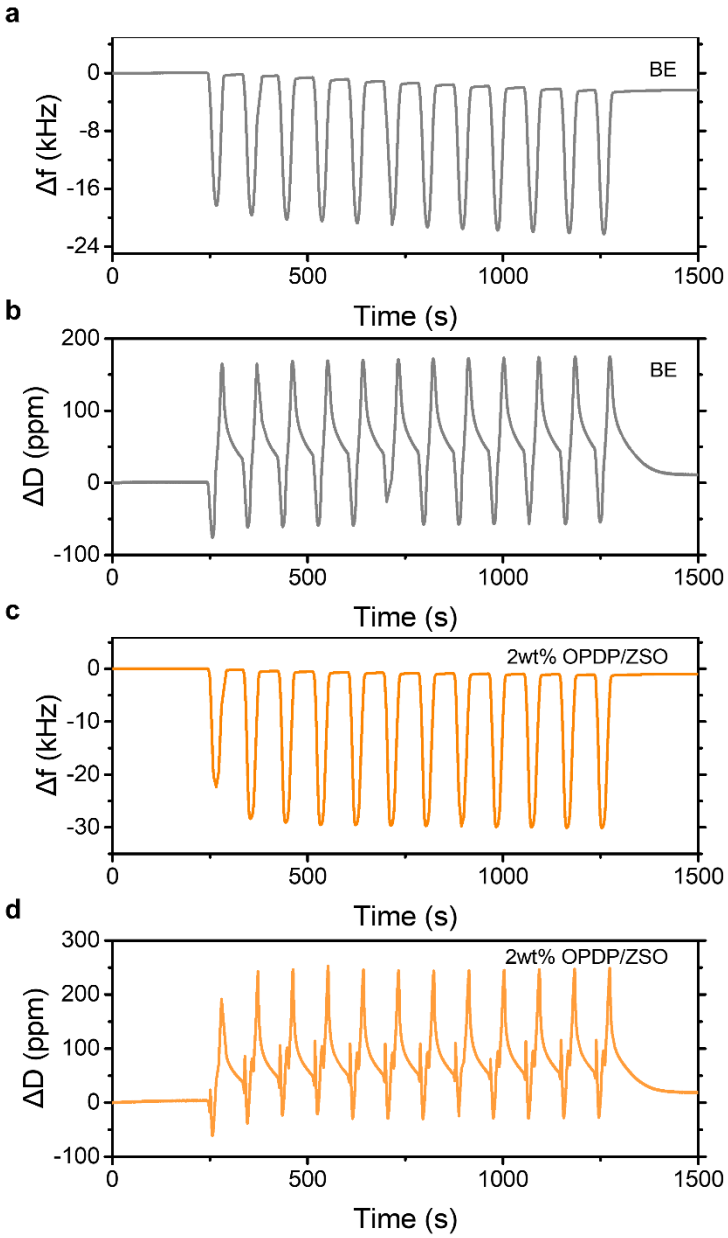

Fig. S30. EQCM-D frequency shifts (Δf, a and c) and dissipation shifts (ΔD, b and d) during the CV cycles in BE and 2 wt% OPDP/ZSO.

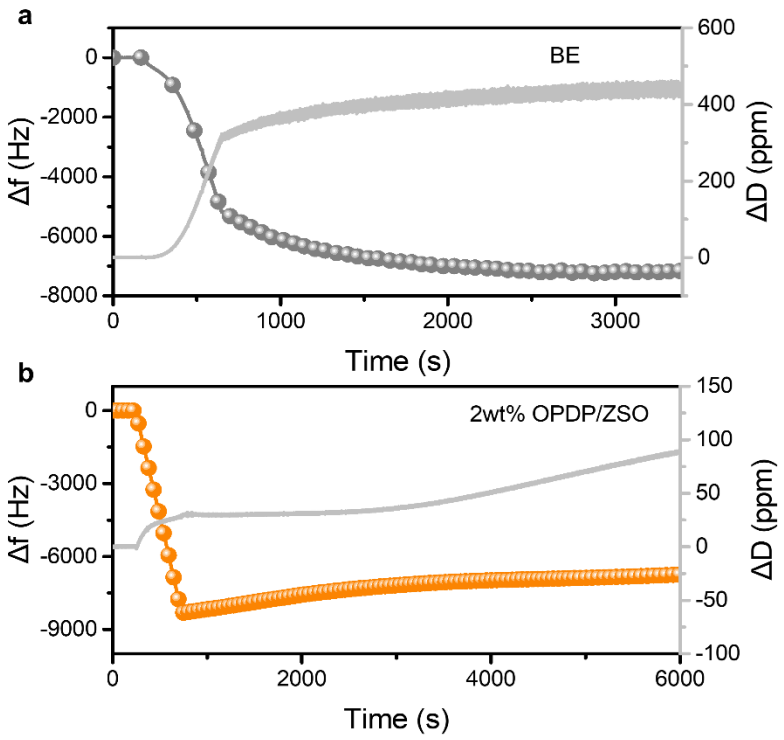

Fig. S31. Time dependence of Δf and ΔD shifts during the deposition and rinsing process in different electrolytes within an 8 min plating procedure at a current density of 0.5 mA cm^{-2}.

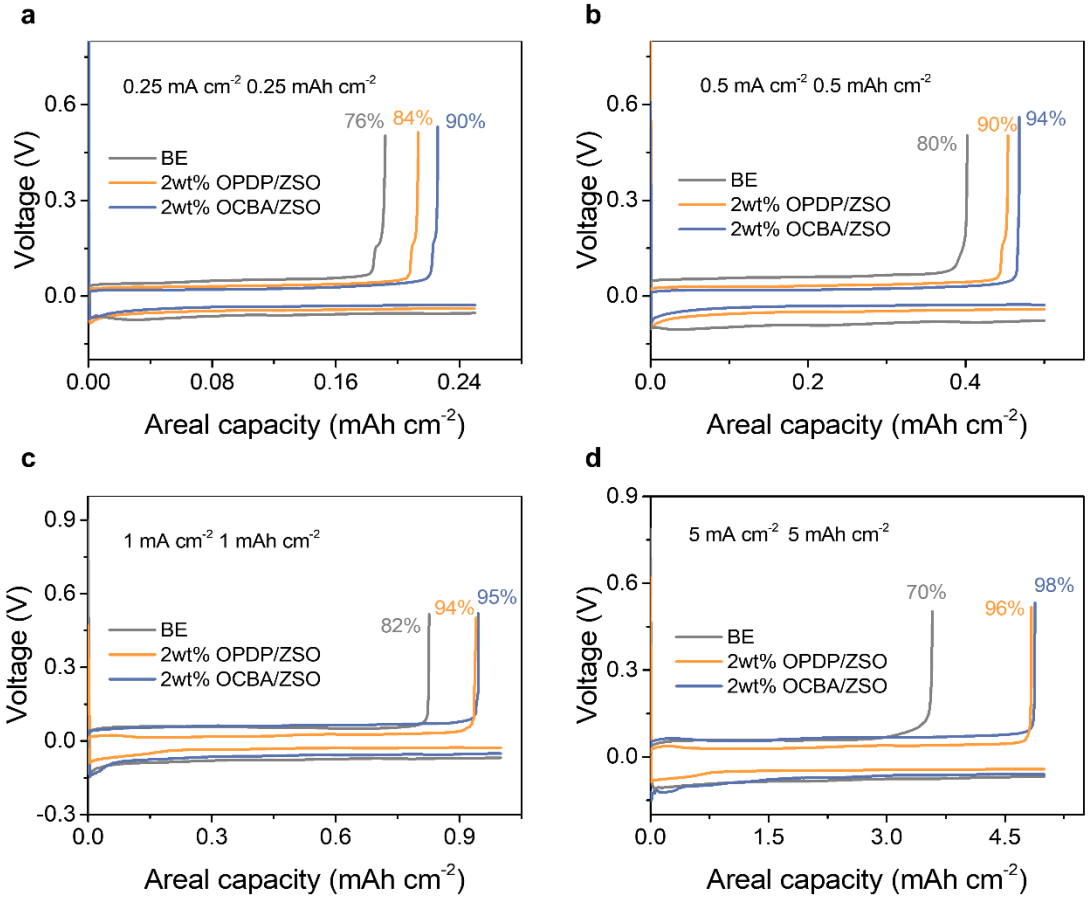

Fig. S32. Initial CE values of Zn//Cu cells with different electrolytes at various current densities.

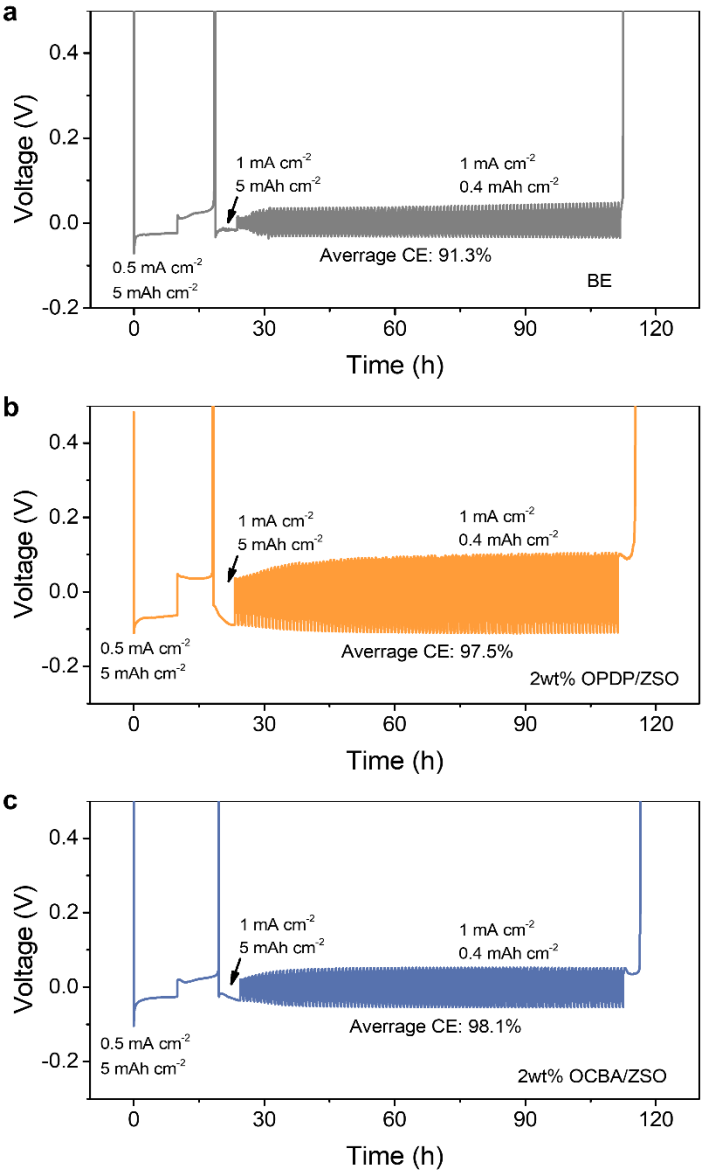

Fig. S33. The average CE measurement by Aurbach method and corresponding polarization profiles in (a) BE, (b) 2 wt% OPDP/ZSO, and (c) 2 wt% OCBA/ZSO.

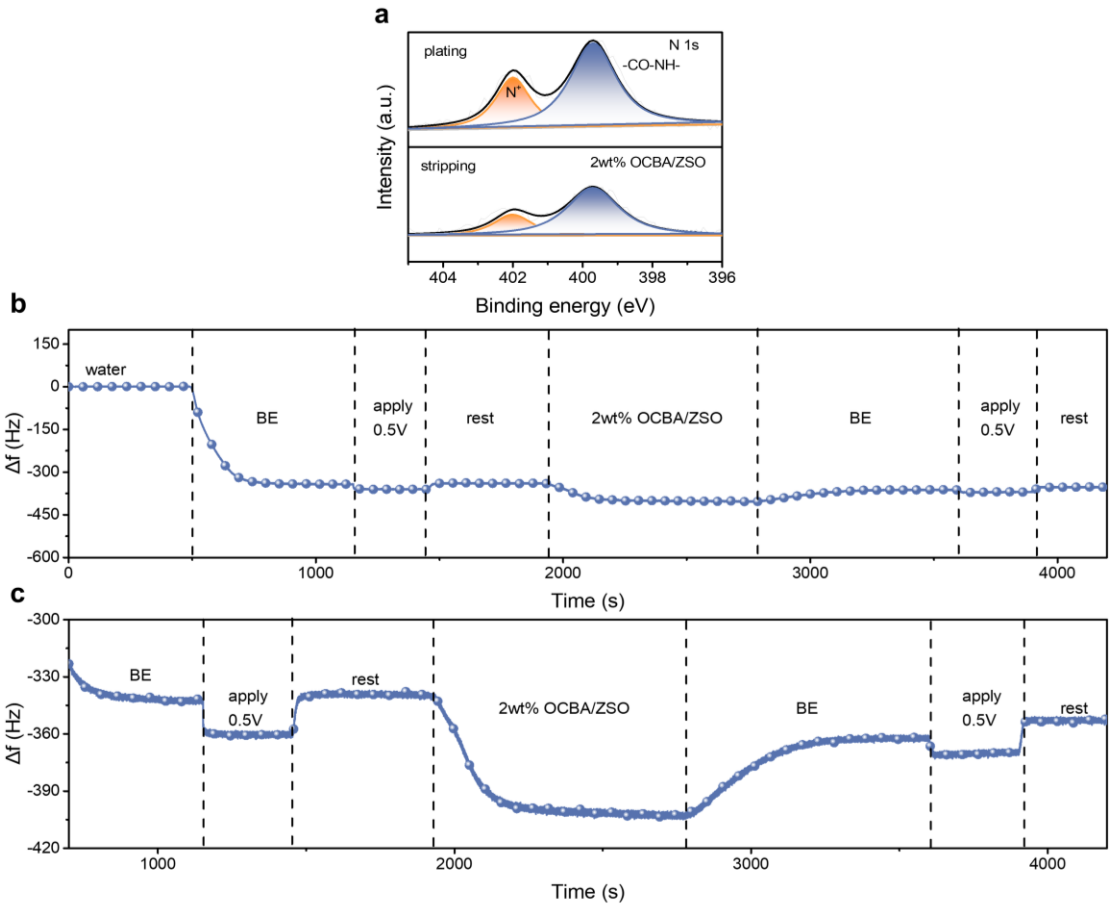

Fig. S34. (a) Deconvoluted XPS data of N 1s region on Zn anodes after a plating or stripping process at a current density of 1 mA cm^{-2} for 10 min in 2 wt% OCBA/ZSO. (b) EQCM-D measurement for evaluating the reversible adsorption/desorption of OCBA. (c) The enlarged view of the 700~4200 s range for Fig. S34b.

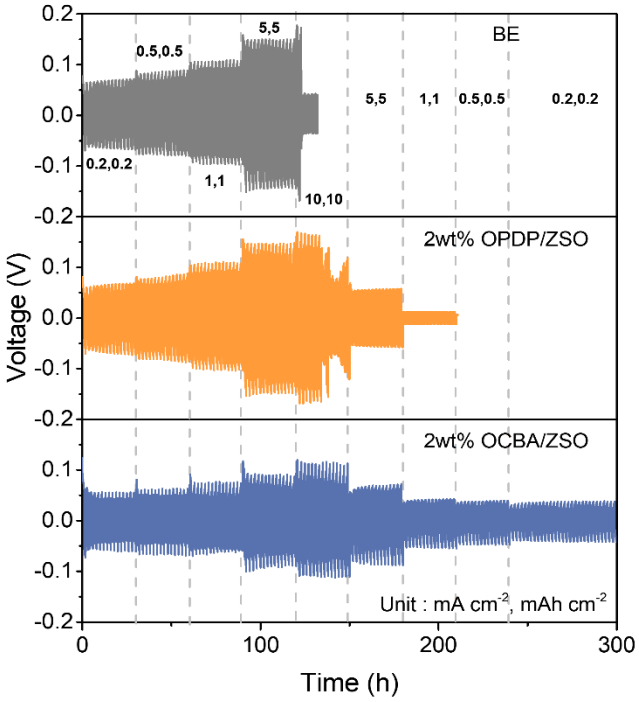

Fig. S35. Rate performance of Zn//Zn cells in different electrolytes.

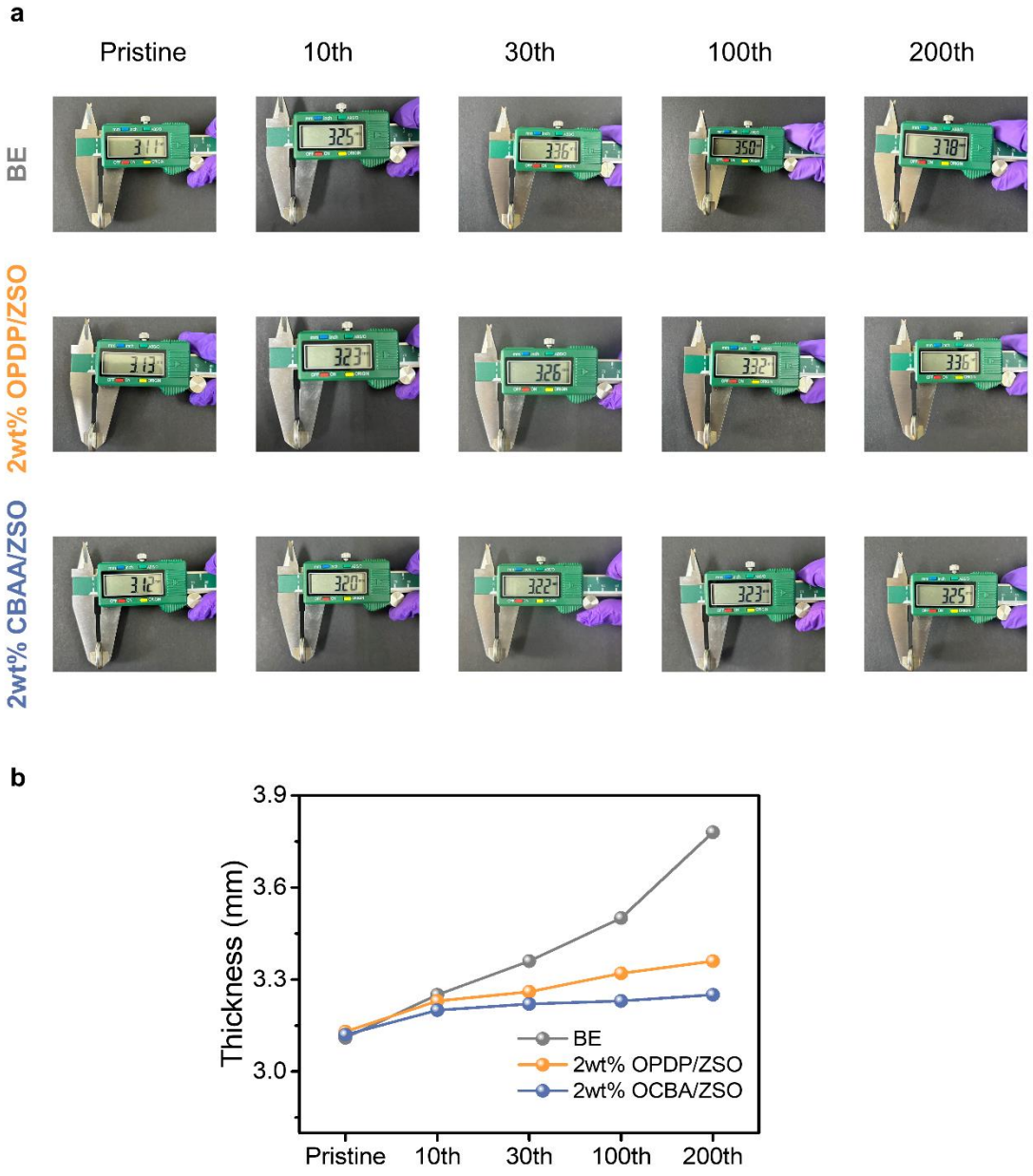

Fig. S36. Comparison of the thickness changes of Zn//Zn batteries with different electrolytes at different cycle stages.

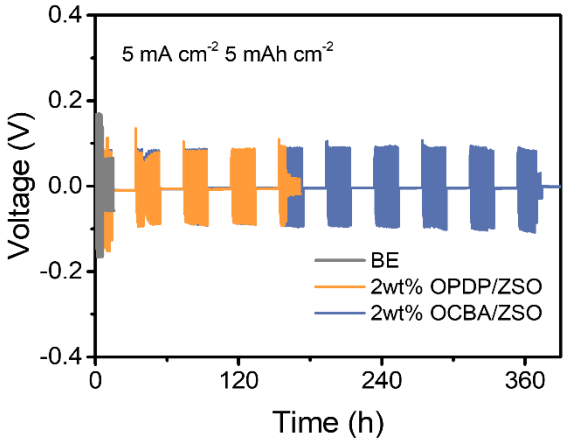

Fig. S37. The shelving-recovery performance of Zn//Zn symmetric cells with different electrolytes under 5 mA cm^{-2} and 5 mAh cm^{-2} with 20 h shelving for every 10 cycles.

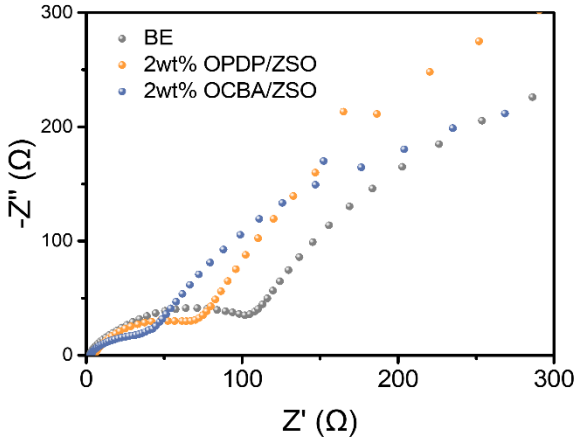

Fig. S38. EIS plots of the Zn//PANI full batteries with different electrolytes.

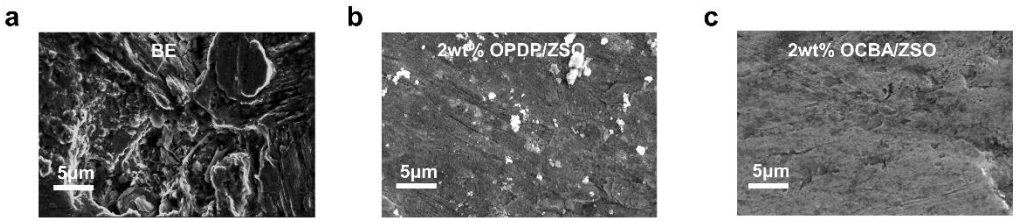

Fig. S39. The SEM images of Zn anodes of Zn//PANI full batteries with (a) BE, (b) 2 wt% OPDP/ZSO, and (c) 2 wt% OCBA/ZSO after 100 cycles.

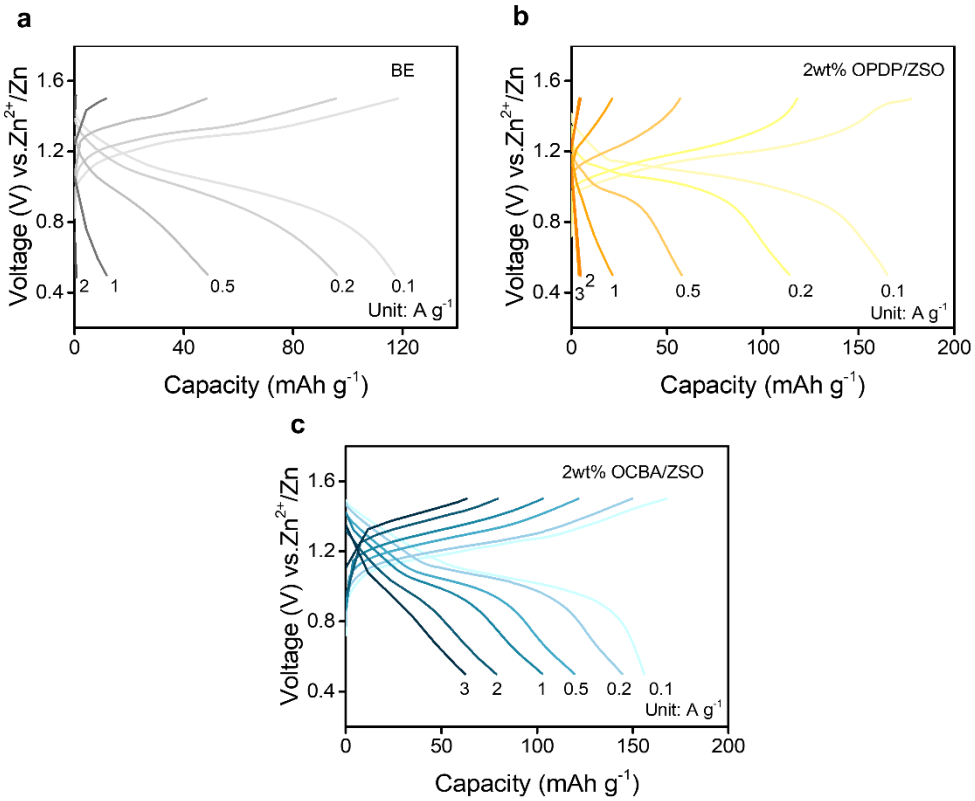

Fig. S40. Charge/discharge curves at different current densities for Zn//PANI cells with (a) BE, (b) 2 wt% OPDP/ZSO, and (c) 2 wt% OCBA/ZSO.

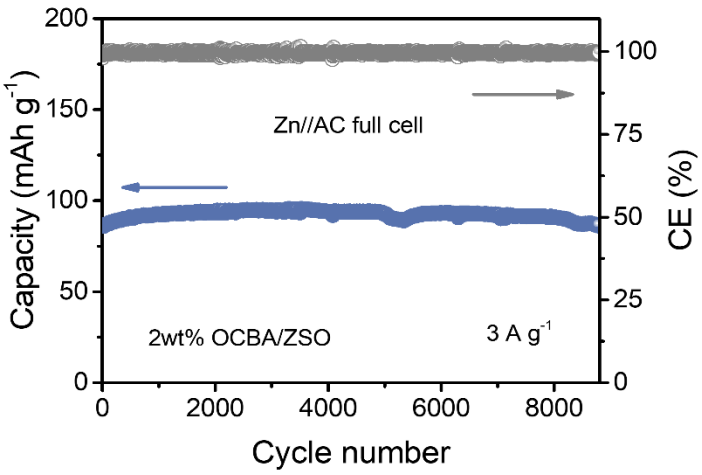

Fig. S41. Cycling stability of a Zn//AC hybrid capacitor with 2 wt% OCBA/ZSO.

Table S1. Performance comparison between the Zn//Zn cell with OCBA additive and the cells with other electrolyte additives at 1 mA cm^{-2} and 1 mAh cm^{-2}.

Test condition	Electrolyte additives*	Lifespan (h)	Ref.
Current density: 1 mA cm^{-2} Areal capacity: 1 mAh cm^{-2}	$C_3N^+COO^-$	3500	3
	locust bean gum	1600	4
	C_8TAB	2500	5
	pyrimidine	3000	6
	[EMIM]OTF	1800	7
	TMB	1800	8
	PMCNA	4500	9
	PDD	3000	10
	ZSS	5500	11
	Val-H	2250	12
	CA	4500	13
	MSA	1300	14
	SAA	3400	15
	silk fibroin	1800	16
	TEG	2700	17
	DMAPS	2100	18
	EMImCl	1700	19
	18-crown-6	500	20
	BIS-TRIS	1200	21
	Silk Sericin	5200	22
	POPSO-Na	1600	23
	AS	3300	24
	Gly	3200	25
	Curcumin	3800	26
	DHP	3000	27
	Methacrylic acid	4000	28
	AChI	3700	29
	OCBA	6660	This work

*The complete designations for the abbreviations listed under the "Electrolyte additives" column are: (carboxymethyl)trimethylammonium ($C_3N^+COO^-$), octyltrimethylammoniumbromide (C_8TAB), 1-ethyl-3-methylimidazole trifluoromethanesulfonate ([EMIM]OTF), Trifluoro((4-methylmorpholino-4-ium) methyl) borate (TMB), zwitterion polymer (PMCNA), polydiallyl dimethylammonium chloride (PDD), 2-acrylamide-2-methylpropanesulfonic acid (ZSS), D-valine-filled all in-one hydrogel (Val-H), citric

acid and asparta (CA), memethylsulfonylamine (MSA), saponin and anisaldehyde (SAA), Triethylene glycol (TEG), sulfonated amphoteric betaine (DMAPS), 1,4,7,10,13,16-hexaoxacyclooctadecane (18-crown-6), 1-ethyl-3-methylimidazolium chloride (EMImCl), 2-Bis(2-hydroxyethyl)amino-2-(hydroxymethyl)-1,3-propanediol (BIS-TRIS), piperazine-N,N-bis(2-hydroxypropanesulfonic acid) sodium salt (POPSO-Na), amikacin sulfate (AS), glycine (Gly), dimethyl hydroxymethylphosphonate (DHP), acetylcholine iodide (AChI).

Table S2. Comparison of electrochemical performance of Zn//PANI pouch batteries of this work with previous reports.

Electrolyte*	Cathode	Current ($A\ g^{-1}$)	Cycle number	Capacity ($mAh\ g^{-1}$)	Ref.
$ZnSO_4$-PEA	Polyaniline	2	300	62.3	30
2 m $Zn(OTF)_2$ + 40 vol.% DG	Polyaniline	0.1	100	98	31
ZG-14/In-30	Polyaniline	0.05	100	80.1	32
PVA/$Zn(CF_3SO_3)_2$ gel	Polyaniline	0.5	200	100	33
2 M $Zn(CF_3SO_3)_2$	Polyaniline	1	200	106.3	34
Anti-M-50%	Polyaniline	0.1	100	96.4	35
DES-4	Polyaniline	0.05	50	130	36
2 wt% OCBA/ZSO	Polyaniline	0.5	150	120.8	This work

*The complete designations for the abbreviations listed under the "Electrolyte" column are: 1-phenylethylamine hydrochloride (PEA), diethylene glycol monoethylether (DG), polyvinyl alcohol (PVA), $Zn(ClO_4)_2 \cdot 6H_2O$, ethylene glycol, and $InCl_3$ (ZG-14/In-30), 50 % methanol by volume (Anti-M-50 %), $ZnCl_2$/ ethylene glycol ratios of 1:4 (DES-4).

Reference

1 Y. Deng, Z. Xiao, W. Xu, Y. Wang, Z. Peng, L. Fei, T. Wang, Moderate yet reversible oligozwitterion adsorption unlocks stable zinc-ion batteries, *Adv. Funct. Mater.,* 2025, e09652.

2 X. Lin, G. Zhou, M. J. Robson, J. Yu, S. C. T. Kwok, F. Ciucci, Hydrated deep eutectic electrolytes for high-performance Zn-ion batteries capable of low-temperature operation, *Adv. Funct. Mater.,* 2022, **32**, 2109322.

3 X. Wu, Y. Xia, S. Chen, Z. Luo, X. Zhang, Y. Lu, H. Pan, B. B. Xu, M. Yan, Y. Jiang, Transient zwitterions dynamics empowered adaptive interface for ultra-stable Zn plating/stripping, *Small,* 2024, **20**, 2306739.

4 K. Wang, H. Zhan, W. Su, X.-X. Liu, X. Sun, Ordered interface regulation at Zn electrodes induced by trace gum additives for high-performance aqueous batteries, *Energy Environ. Sci.,* 2025, **18**, 1398-1407.

5 D. Tang, X. Zhang, D. Han, C. Cui, Z. Han, L. Wang, Z. Li, B. Zhang, Y. Liu, Z. Weng, Q.-H. Yang, Switching hydrophobic interface with ionic valves for reversible zinc batteries, *Adv. Mater.,* 2024, **36**, 2406071.

6 D. Cai, H. Cheng, J.-L. Yang, H. Liu, T. Xiao, X. Liu, M. Chen, H. J. Fan, Understanding the structure–activity relationship of additives for durable zn metal batteries: A case study of aromatic molecules, *Energy Environ. Sci.,* 2024, **17**, 8349-8359.

7 J. Weng, W. Zhu, K. Yu, J. Luo, M. Chen, L. Li, Y. Zhuang, K. Xia, Z. Lu, Y. Hu, C. Yang, M. Wu, Z. Zou, Enhancing Zn-metal anode stability: Key effects of electrolyte additives on ion-shield-like electrical double layer and stable solid electrolyte interphase, *Adv. Funct. Mater.,* 2024, **34**, 2314347.

8 Z. Zha, T. Sun, D. Li, T. Ma, W. Zhang, Z. Tao, Zwitterion as electrical double layer regulator to in-situ formation of fluorinated interphase towards stable zinc anode, *Energy Storage Mater.,* 2024, **64**, 103059.

9 D. Feng, Y. Jiao, P. Wu, Guiding zn uniform deposition with polymer additives for long-lasting and highly utilized Zn metal anodes, *Angew. Chem. Int. Ed.,* 2023, **62**, e202314456.

10 M. Peng, X. Tang, K. Xiao, T. Hu, K. Yuan, Y. Chen, Polycation-regulated electrolyte and interfacial electric fields for stable zinc metal batteries, *Angew. Chem. Int. Ed.,* 2023, **62**, e202302701.

11 T. Long, Q. Zhao, G. Yin, P. Xie, S. Liu, X. Ma, Q. Wu, B. Lu, Z. Dai, X. Zeng, Regulating interfacial ion adsorption for smooth and durable zinc cycling at high area capacity, *Adv. Funct. Mater.,* 2024, **34**, 2315539.

12 J. Lin, C. Ji, G. Guo, Y. Luo, P. Huang, F. Xu, L. Sun, W. Pfleging, K. S. Novoselov, Interfacial h-bond network/concentration fields/electric fields regulation achieved by D-valine anions realizes the highly efficient aqueous zinc ion batteries, *Angew. Chem. Int. Ed.,* 2025, **64**, e202501721.

13 T. Xue, Y. Mu, Z. Zhang, J. Guan, J. Qiu, C. Yang, L. Zang, L. Zeng, Enhanced zinc deposition and dendrite suppression in aqueous zinc-ion batteries via citric acid-aspartame electrolyte additives, *Adv. Energy Mater.,* 2025, **15**, 2500674.

14 X. Wei, Y. Mu, J. Chen, Y. Zhou, Y. Chu, L. Yang, C. Huang, T. Xue, L. Zang, C. Yang, L. Zeng, Optimizing Zn (100) deposition via crystal plane shielding effect towards ultra-high rate and stable zinc anode, *Energy Storage Mater.,* 2025, **75**, 104026.

15 K. Liu, M. Sun, Y. Wu, T. Zhang, A. Zhu, S. Bu, C. Luan, K. Liu, Y. Zhou, D. Lin, S. Wu, C. S. Lee, B. Huang, G. Hong, W. Zhang, Binary electrolyte additive-reinforced interfacial molecule adsorption layer for ultra-stable zinc metal anodes, *Adv. Mater.,* 2025, **37**, 2420079.

16 L. Zhang, Y. Han, Y. Geng, H. Zhang, H. Liu, Y. He, Z. Yan, Z. Zhu, Aqueous zinc-ion batteries

with boosted stability and kinetics under a wide temperature range, *Angew. Chem. Int. Ed.,* 2025, **64**, e202500434.

17 F. Wu, J. Zhang, L. Ma, P. Ruan, Y. Chen, S. Meng, R. Yin, W. Shi, W. Liu, J. Zhou, X. Cao, Directing zn growth with biased adsorption of straight-chain molecules for superior Zn anode stability, *Angew. Chem. Int. Ed.,* 2025, **64**, e202421787.

18 X. Wang, H. Peng, H. Zheng, Z. Liu, K. Sun, G. Ma, Z. Lei, Weak solvation effects and molecular-rich layers induced water-poor helmholtz layers boost highly stable Zn anode, *Energy Storage Mater.,* 2024, **73**, 103856.

19 Q. Zhang, Y. Ma, Y. Lu, X. Zhou, L. Lin, L. Li, Z. Yan, Q. Zhao, K. Zhang, J. Chen, Designing anion-type water-free Zn^{2+} solvation structure for robust Zn metal anode, *Angew. Chem. Int. Ed.,* 2021, **60**, 23357-23364.

20 A. Wu, S. Zhang, Q. Li, W. Xue, C. Li, B. Xi, W. Mao, K. Bao, S. Xiong, Multifunctional crown ether additive regulates desolvation process to achieve highly reversible zinc-metal batteries, *Adv. Energy Mater.,* 2025, **15**, 2404450.

21 M. Luo, C. Wang, H. Lu, Y. Lu, B. B. Xu, W. Sun, H. Pan, M. Yan, Y. Jiang, Dendrite-free zinc anode enabled by zinc-chelating chemistry, *Energy Storage Mater.,* 2021, **41**, 515-521.

22 Y. Xiong, W. Teng, Z. Zhao, S. Xu, Y. Ma, Y. Gong, D. Li, X. Wang, Y. Shen, Z. Shen, Y. Hu, Effective control of the solution environment in aqueous zinc-ion batteries for promoting (002)-textured zinc growth by a bio-electrolyte additive, *Energy Storage Mater.,* 2025, **74**, 103959.

23 H. Peng, D. Wang, X. Wang, W. Miao, J. Zeng, B. Tao, Y. Li, Y. Tang, G. Ma, Coupling solvation structure regulation and interface engineering via reverse micelle strategy toward highly stable Zn metal anode, *Adv. Funct. Mater.*, 2025, **35**, 2417695.

24 Z. Chen, R. Jiang, Y. Chen, H. Zhu, X. Tang, X. Huang, Y. Xie, J. Li, C. Zhang, L. Chen, W. Wei, L. Zhou, Zincophilic group-rich aminoglycosides for ultra-long life and high-rate zinc batteries, *Energy Storage Mater.,* 2025, **74**, 103913.

25 Y. Liu, Y. An, L. Wu, J. Sun, F. Xiong, H. Tang, S. Chen, Y. Guo, L. Zhang, Q. An, L. Mai, Interfacial chemistry modulation via amphoteric glycine for a highly reversible zinc anode, *ACS Nano,* 2023, **17**, 552-560.

26 J. Zhang, Q. Wu, X. Liu, S. Yang, F. Luo, Z. Yan, J. Huang, Y. Chen, Nanomicellar electrolyte enables highly reversible zinc anode via strengthening symmetric plating/stripping chemistry, *Adv. Funct. Mater.*, 2025, e20448.

27 H. Tan, C. Meng, Y.-P. Zhang, J.-Y. Zhao, H. Chen, L. Chen, Z.-H. Yin, X.-L. Wu, H. Liu, J.-J. Wang, Decoupling of ion-solvent interactions via compartmentalized molecular design for ultra-stable aqueous zinc batteries, *Adv. Funct. Mater.*, 2025, e16270.

28 N. Yu, S. Lin, S. Zhou, Y. Li, J. Li, Q. Zeng, L. Chen, L. Wang, K. Guo, X. Wang, Y. Li, Engineering aqueous electrolytes with a trifunctional additive for robust zinc anodes across a wide temperature range, *Energy Storage Mater.,* 2025, **80**, 104398.

29 J. Li, X. Zhang, X. Xu, B. Xie, Y. Wang, L. Su, H. Wang, C. Ouyang, X. Gao, Cation-engineered gradient interfacial structure toward dendrite-free and shuttle-free aqueous Zn-iodine batteries, *Adv. Sci.,* 2025, **12**, e09239.

30 M. Wang, Y. Cheng, H. Zhao, J. Gao, J. Li, Y. Wang, J. Qiu, H. Zhang, X. Chen, Y. Wei, A multifunctional organic electrolyte additive for aqueous zinc ion batteries based on polyaniline cathode, *Small,* 2023, **19**, 2302105.

31 R. Wang, Q. Ma, L. Zhang, Z. Liu, J. Wan, J. Mao, H. Li, S. Zhang, J. Hao, L. Zhang, C. Zhang, An

aqueous electrolyte regulator for highly stable zinc anode under −35 to 65°C, *Adv. Energy Mater.,* 2023, **13**, 2302543.

32 J. Wan, R. Wang, Z. Liu, S. Zhang, J. Hao, J. Mao, H. Li, D. Chao, L. Zhang, C. Zhang, Hydrated eutectic electrolyte induced bilayer interphase for high-performance aqueous Zn-ion batteries with 100°C wide-temperature range, *Adv. Mater.,* 2024, **36**, 2310623.

33 F. Wan, L. Zhang, X. Wang, S. Bi, Z. Niu, J. Chen, An aqueous rechargeable zinc-organic battery with hybrid mechanism, *Adv. Funct. Mater.,* 2018, **28**, 1804975.

34 W. Shao, D. Zhang, J. Zhang, N. Fu, Q. Chen, Z. Yang, Interfacial energy-level modulation enables electron-ion decoupling for hydrogen suppression and highly durable zinc metal anodes, *Adv. Funct. Mater.*, 2025, e28181.

35 J. Hao, L. Yuan, C. Ye, D. Chao, K. Davey, Z. Guo, S.-Z. Qiao, Boosting zinc electrode reversibility in aqueous electrolytes by using low-cost antisolvents, *Angew. Chem. Int. Ed.,* 2021, **60**, 7366-7375.

36 L. Geng, J. Meng, X. Wang, C. Han, K. Han, Z. Xiao, M. Huang, P. Xu, L. Zhang, L. Zhou, L. Mai, Eutectic electrolyte with unique solvation structure for high-performance zinc-ion batteries, *Angew. Chem. Int. Ed.,* 2022, **61**, e202206717.